



Microscale layering of liquid and vapor phases within microstructures for a new generation two-phase heat sink



Abdolreza Fazeli, Sajjad Bigham, Saeed Moghaddam*

Department of Mechanical and Aerospace Engineering, University of Florida, Gainesville, FL 32611, United States

ARTICLE INFO

Article history:

Received 17 September 2015

Received in revised form 29 November 2015

Accepted 2 December 2015

Available online 24 December 2015

ABSTRACT

In this study, a new heat sink architecture is introduced that operates at two different phase change heat transfer modes. At low wall superheat temperatures, the heat sink operates under the thin film evaporation heat transfer mode and then transitions to the boiling heat transfer mode when the wall superheat temperature increases. This unique function is enabled through constraining the liquid and vapor phases into separate domains using a capillary-controlled meniscus formed within a hierarchical 3D structure. The structure is designed to form thin liquid layers between vertically oriented menisci across which the liquid is evaporated into neighboring vapor channels. The entire structure is then capped by a hydrophobic vapor-permeable membrane to fully confine the liquid layers while allowing vapor to pass through the membrane. At low wall superheats, the liquid layers directly evaporate into the vapor channels. In this operation mode, the heat flux was linearly increased to a maximum of 54 W/cm^2 at approximately $8 \text{ }^\circ\text{C}$ wall superheat temperature, corresponding to a heat transfer coefficient of approximately $62 \text{ kW/m}^2 \text{ K}$. The heat transfer coefficient only slightly declined with increasing the wall superheat temperature but substantially improved as the liquid supply pressure was increased. Increasing the superheat temperature beyond $7\text{--}9 \text{ }^\circ\text{C}$ resulted in transition to the boiling heat transfer mode with a pronounced increase in surface temperature fluctuations. This transition to boiling results in a decline in the heat transfer coefficient because the meniscus formed between the liquid and vapor spaces breaks down. However, the heat removal capacity is significantly increased, and a critical heat flux of about 300 W/cm^2 is reached at $<30 \text{ }^\circ\text{C}$ wall superheat temperature, corresponding to a heat transfer coefficient of approximately $100 \text{ kW/m}^2 \text{ K}$.

Published by Elsevier Ltd.

1. Introduction

The ever-increasing demand for performance improvement and miniaturization of electronics has led to significant generation of waste heat that must be effectively dissipated to ensure a reliable device operation [1,2]. Traditional heat sinks are no longer capable of dissipating the generated heat and innovative approaches are needed to address the emerging thermal management challenges [3–5].

Among different cooling approaches, boiling in microchannels has received significant attention due to benefits of the phase change process that include a nearly constant fluid temperature along the flow stream, a high heat transfer coefficient, and a low fluid flow rate at a high vapor exit quality. Prior studies on two-phase microchannel heat sinks have shown promise in achieving high heat transfer coefficients and heat fluxes through implementation of surface structures and variations in surface-liquid

interfacial properties [6–13]. Kuo and Peles [9] utilized artificial reentrant cavities on microchannels walls to increase the heat transfer coefficient and reduce instabilities. Nanowires employed on microchannels walls have been shown [10,12] to increase the heat transfer coefficient and delay surface dryout and the onset of flow instability. More recently, implementation of a vapor venting membrane over microchannels has been proposed to alter two-phase flow thermohydraulic characteristics through removing bubbles from the flow [11,13]. Notably, Fazeli et al. [13] implemented a vapor-permeable hydrophobic membrane over microchannels to constrain liquid while allowing vapor to exit. This new approach did not suffer from the limitations associated with a conventional venting device [14] and allowed altering dynamics of the critical heat flux (CHF) by limiting the bubbles growth over the heat transfer surface through subjecting them to an omnidirectional pressure and subsequently ejecting them through the membrane. A proof-of-concept device developed by Fazeli et al. [13] achieved a heat removal capability of 370 W/cm^2 at a wall superheat of less than $25 \text{ }^\circ\text{C}$.

* Corresponding author.

E-mail address: saeedmog@ufl.edu (S. Moghaddam).

Further performance and operational issues must be resolved to facilitate implementation of two-phase cooling systems in real applications. Typically, experimental boiling loops studied in laboratory settings are carefully controlled and conditioned to reach boiling point and consequently achieve the performance benefits associated with the phase change process (i.e. high heat transfer coefficient, near isothermal conditions, low mass flow rate, etc.). Often times, a similar approach is not practical in an application. In situations with rapid startups and frequent on and off cycling, significant changes in cooling characteristics of the heat sink can occur. To address issues associated with such circumstances, alternative heat sink designs must be developed.

Alternative microchannel heat sink designs could be realized if the boiling sub-processes are better understood and carefully controlled. Microscale boiling studies have shown that the boiling heat transfer process consists of sub-mechanisms with fundamentally different physical nature [15–20]. Moghaddam and Kiger [16,17] investigated the dynamics of heat transfer during nucleate pool boiling process and showed that three distinctly different mechanisms of heat transfer are active at the surface. They showed that the microlayer evaporation process is the most effective mode of heat transfer and can dissipate heat flux at a substantially higher rate compared to other mechanisms (i.e. transient conduction and microconvection). Recently, Bigham and Moghaddam [20,37] have shown that the heat transfer rate associated with the thin film evaporation process is greater than the average surface heat flux in the microchannel flow boiling process. It has been shown that the microlayer evaporation mode of heat transfer occurs only for a very short period of time and over a limited fraction of the heat transfer surface area [16,17,20,37]. Thus, the overall contribution of this effective mode of heat transfer remains limited.

In this work, a phase change heat sink is introduced that operates at two heat transfer modes employing fundamentally different operational principles. At low wall superheat temperatures, the surface structures form vertically orientated capillary-controlled menisci, thus allowing the heat sink to operate under the thin film evaporation mode. As wall superheat increases, nucleate boiling occurs and the menisci break down. In this mode, the liquid pressure acting on the generated bubbles limits their lateral expansion during the bubbling events and forces them to exit through a vapor-permeable membrane bonded directly on the structure. In the following sections, first, fundamentals of the new concept are introduced and then a device fabricated based on the proposed concept is presented. The thermal performance of the heat sink is then experimentally and numerically studied.

2. Concept

Fig. 1 shows a schematic of the heat sink. As the working fluid flows into the liquid microchannels, the capillary forces acting between pillars that separate the liquid and vapor channels form menisci that prevent liquid entry into the vapor channels. The menisci planes are normal to the base of the heated surface enabling enhancements of the total evaporation surface area through increasing the micro-posts height (cf. Fig. 1). Unlike the conventional phase change heat sinks, this heat sink has no liquid outlet; ensuring a 100% exit vapor quality at any heat load.

The Young–Laplace equation governs the relation between the maximum liquid pressure held by the interface and the microstructure geometry:

$$\Delta P = P_l - P_v = \sigma_f \cos \theta_A (1/R_1 + 1/R_2) \quad (1)$$

where σ_f is the water surface tension, θ_A is the advancing contact angle, R_1 and R_2 are the principle radii of curvature and P_l and P_v denote liquid and vapor pressures, respectively. It is clear that

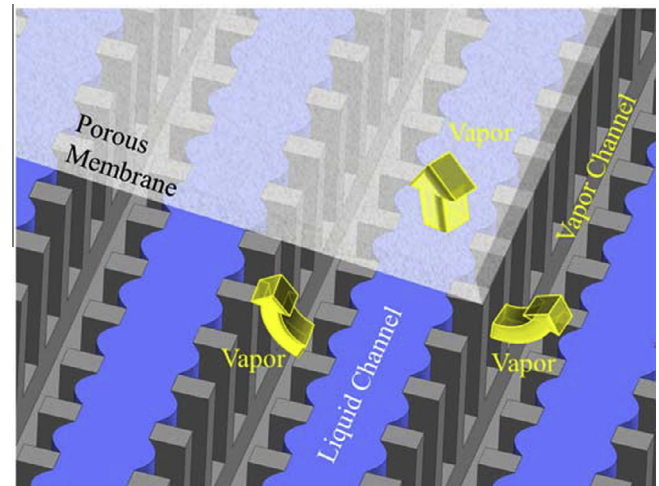


Fig. 1. A schematic showing the liquid and vapor domains and flow arrangement within the heat sink.

decreasing the spacing between the posts increases the meniscus breakthrough pressure.

At low wall superheats, the vertically oriented thin films directly evaporate into the vapor channel. As the wall superheat increases, nucleation begins within the liquid channels and the liquid–vapor interface ruptures as a result. Consequently, the liquid wets the entire heat sink and the dominant heat transfer mode changes to boiling. Fig. 2 shows the operational principle of the heat sink in the boiling mode. As depicted, the omnidirectional pressure forces applied on the bubbles limit their lateral expansion and push them through the vapor permeable membrane assembled on the micro-posts.

3. Numerical procedure

A set of numerical simulations was conducted to study the thermo-hydraulic characteristics of the heat sink. The computational domain highlighted in green in Fig. 3 resembles the space between two posts, where the meniscus (i.e. liquid–vapor interface) forms. The computational domain is discretized by structured hexahedron mesh (cf. Fig. 4). The liquid and vapor phases are separated by an interface (ABCDEA plane in Fig. 4) through which the phase change process occurs. The interface temperature has been fixed at the saturation temperature corresponding to the system pressure at the interface [21]. The mass transfer rate at the liquid–vapor interface is equal to the net balance of heat transfer between the liquid and vapor phases divided by the latent heat of vaporization [22].

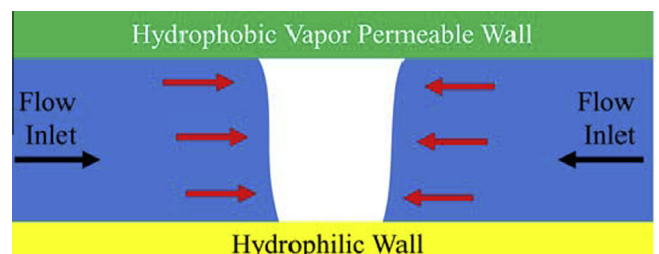


Fig. 2. Schematic of a bubble interfacing a hydrophobic vapor venting membrane while under omnidirectional pressure.

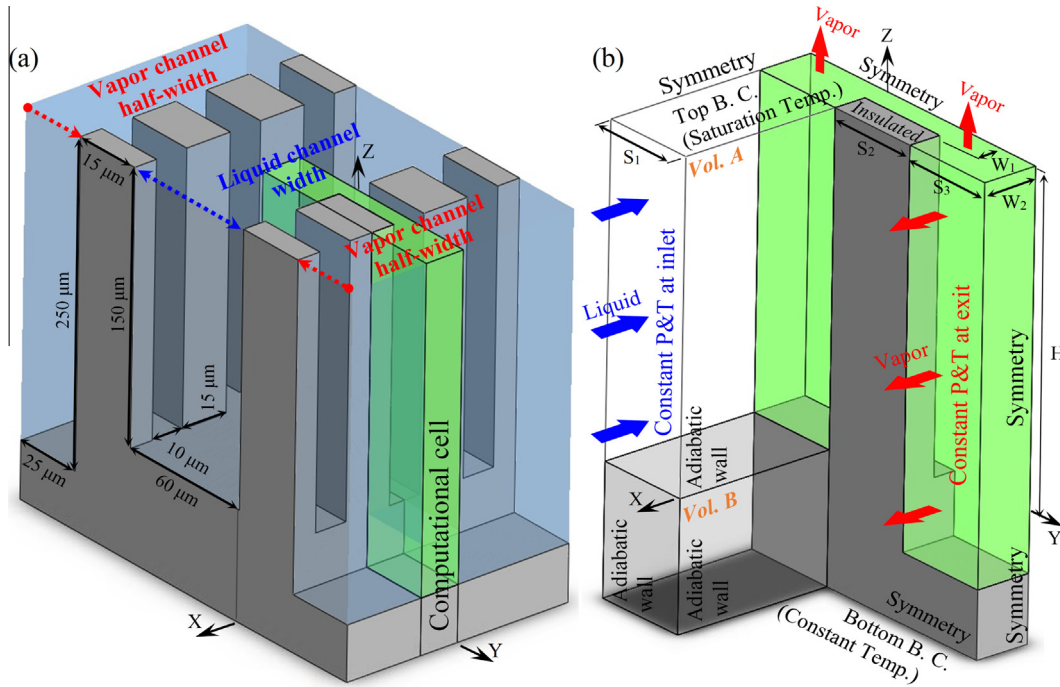


Fig. 3. (a) Location of the computational cell with respect to the liquid and vapor channels, (b) a closed view of the computational cell along with the conditions used at each boundary.

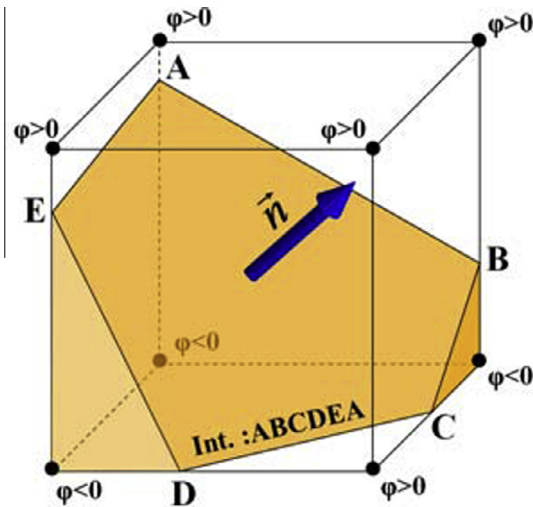


Fig. 4. A representative hexahedron computational cell, ABCDEA is the liquid-vapor interface.

$$\dot{m}_{evap} = \left(\frac{-k_{liq} \nabla T \cdot \vec{n} + k_{vap} \nabla T \cdot \vec{n}}{h_{fg}} \right) \frac{A_{interface}}{V_{cell}} \quad (2)$$

where n is the interface normal vector, $A_{interface}$ is the interface area located within the computational cell and V_{cell} is the cell volume (cf. Fig. 4). To accurately estimate spatial gradients at the interface, the Level-Set method [23–25] is utilized. In the Level-Set method, the interface motion is captured by a convection equation for a Level-Set function, ϕ , with a zero value that separates the vapor phase ($\phi > 0$) from the liquid phase ($\phi < 0$):

$$\frac{\partial \phi}{\partial t} + \vec{v} \cdot \nabla \phi = 0 \quad (3)$$

In this study, the level-set method has been utilized only to compute spatial gradients necessary in calculation of the evaporation rate and the surface tension forces at the interface. To track

the liquid and vapor volume fractions in each cell over the entire computational domain, the Volume of Fluid (VOF) method [26–28] has been employed. In this method, a convection equation is used to calculate the liquid volume fraction, α_l , as:

$$\frac{\partial}{\partial t} (\alpha_l \rho_l) + \vec{v} \cdot \nabla (\alpha_l \rho_l) = \dot{m}_{evap} \quad (4)$$

The volume conservation in each cell dictates the vapor volume fraction to be $\alpha_v = 1 - \alpha_l$. Since the volume fraction values do not uniquely identify the interface between the phases, an interface reconstruction scheme is needed. In the present study, the piecewise linear geometric reconstruction scheme [29,30] available in FLUENT [31] is employed to update the volume fraction values in each cell through a reconstruction step followed by a propagation step. In the reconstruction step, the orientation of the segment that divides each cell into the vapor and liquid domains is calculated. In the propagation step, the volume of a particular fluid through a mixture cell face during a time step is computed and the volume of the fraction field at the new time is updated. In the proposed design (with the length scales of 10–150 μm), the effect of gravitational forces is found to be negligible with respect to the surface tension forces (Bond number, $Bo = \rho g L^2 / \sigma \sim 10^{-5} - 10^{-3}$) and thus is not taken into account in the numerical simulation. To consider the surface tension forces, a continuum surface force (CSF) model [32] has been utilized. The surface tension force can be converted into a volumetric force using the divergence theorem:

$$F_{vol} = \frac{2\sigma \rho \kappa \nabla \alpha_l}{(\rho_l + \rho_v)} \quad (5)$$

where σ is the surface tension, ρ is the volume-fraction-averaged density ($\rho = \alpha_v \rho_v + \alpha_l \rho_l$) in the computational cell and κ is the interface curvature calculated as the divergence of the normal vector:

$$\kappa = \nabla \cdot \frac{\nabla \alpha_l}{|\nabla \alpha_l|} \quad (6)$$

This volumetric force then becomes a source for the momentum equation as shown in the equation provided below:

$$\frac{\partial}{\partial t}(\rho\vec{v}) + \nabla \cdot (\rho\vec{v}\vec{v}) = -\nabla p + \nabla \cdot [\mu(\nabla\vec{v})] + F_{vol} \quad (7)$$

A finite-volume based solver, FLUENT, has been employed to solve this problem. The evaporation model (Eq. (2)) is implemented via a User-Defined Function (UDF) written in C code and is capable of parallel computing. In the UDF, first, computational cells located at the interface are detected. The interfacial computational cell has at least one node with a different sign for the level set function compared to other nodes. Then, the interface plane (ABCD plane in Fig. 4) and its normal direction (\vec{n}) are determined. The temperature gradient normal to the interface ($\nabla T \cdot \vec{n}$) and the interface area within the cells are subsequently calculated. Finally, the mass transfer rate associated with phase change at the interface cells (Eq. (2)) is computed.

The position of the computational cell with respect to the liquid and vapor channels is schematically shown in Fig. 3a. The cell is extended from the middle of the liquid channel to the middle of the vapor channel in the Y-direction, and from the middle of the gap between the pillars to the center of the pillars in the X-direction. A close view of the computational cell along with the boundary conditions is presented in Fig. 3b. To ensure that the flow inside the cell is thermally and hydrodynamically developed, entry-length volumes (volume A and B in Fig. 3b) with a sufficient flow length are added to the computational cell. The liquid enters the cell at the saturation temperature. Heat flux continuity is applied at the fluid–solid interfaces (Eq. (8)). The liquid temperature at its interface with the membrane is set at saturation. However, since the membrane is bonded on the pillars by an epoxy, an insulation boundary condition is assumed on the top surface of the pillars. The symmetry and adiabatic boundary conditions are shown in Fig. 3b.

$$k_{fluid} \frac{\partial T}{\partial n} = -k_{solid} \frac{\partial T}{\partial n} \quad (8)$$

The flow field is discretized by a uniform computational grid at a size of 0.2 μm in all three directions. A grid independence study was performed to ensure that the computational results are independent of the grid size. The maximum error in calculations of the local wall heat flux and evaporative mass flux were found to be less than 3% when the grid size was reduced by a factor of 2.

It should be noted that the simulations are aimed at evaluating the heat sink performance under the thin film evaporation mode where formation of quasi-stationary menisci allows implementation of the evaporation model (Eq. (2)). The stochastic nature of the nucleation events and challenges of simulating the bubble growth and departure from the heat transfer surface and their subsequent exit through the permeable membrane involves significant complexity and is beyond the scope of this study.

The UF NESL Sandy-Bridge cluster has been employed to perform the calculations. The cluster is a high performance server with hexa core Intel Xeon E5-2620 processors. In this work, all simulations are conducted with 96 parallel cores to reduce the computational time.

4. Experiments

4.1. Adiabatic test

In order to study the behavior of the liquid–vapor interface in the proposed microstructure, a set of visualization experiments is conducted using a transparent MEMS device made of polydimethylsiloxane (PDMS). The device is fabricated using soft-lithography techniques. Table 1 provides the device dimensions. Fig. 5 shows a schematic of the experimental setup. Water is pumped into the device and the interface position at different

Table 1
Geometrical dimensions of micro-fabricated device.

Channel height, H (μm)	150
Liquid channel width, $2 \times S_1^a$ (μm)	60
Fin width, S_2^a (μm)	15
Vapor channel width, $2 \times S_3^a$ (μm)	50
Gap width, $2 \times W_1^a$ (μm)	10
Center to center pillar spacing, $2 \times W_2^a$ (μm)	25

^a cf. Fig. 3b.

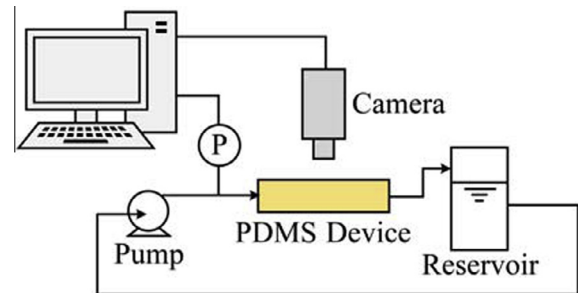


Fig. 5. A schematic of the experimental setup used for adiabatic tests.

supplied liquid pressures is captured using a Nikon LV100 microscope. The images are captured from the topside of the device while the field of view is focused on the microchannel mid-height ($z = 75 \mu\text{m}$).

4.2. Diabatic tests

Fig. 6 shows a heat sink architecture fabricated based on the concept discussed in the previous sections. The device is made on a silicon substrate through a multistep microfabrication process. There are two types of microchannels within the heat sink (cf. Fig. 6d); channels with a liquid inlet (i.e. liquid channels) and channels without a liquid inlet (i.e. vapor channels). The liquid and vapor microchannels are designed such that their respective pressure drop is one order of magnitude smaller than the pressure required to break the meniscus. Considering a high vapor to liquid volume ratio, vapor channels are etched 100 μm deeper than the liquid channels to reduce the vapor phase pressure drop. A 50- μm -thick hydrophobic (with a 140° contact angle with water) nanofibrous PTFE membrane (Pall Corporation, NY) with a 1 μm nominal pore size, and 80% porosity is bonded over the surface structures. The inset in Fig. 6b shows a SEM image of the membrane.

Heat is supplied to the backside of the heat sink active area ($5 \times 5 \text{ mm}^2$) by thin film platinum heaters fabricated using a standard photolithographic process. A set of platinum thin film resistance temperature detectors (RTDs) is similarly fabricated within the heater plane. The sensors are calibrated in an oven with an accuracy of $\pm 0.15 \text{ }^\circ\text{C}$. Temperature of the base of the fins is calculated using the applied heat flux and the known thickness and thermal conductivity of the wall. Dimensions of the micro-fabricated device are similar to those of the adiabatic device provided in Table 1.

The device is tested in a custom made vacuum chamber in which the pressure and temperature were controlled (cf. Fig. 7). Tests were conducted at 100 kPa absolute pressure corresponding to $T_{sat} \sim 99.6 \text{ }^\circ\text{C}$. Distilled water is delivered to the heat sink through a piezoelectric micropump (Model MP6, manufactured by Bartels Mikrotechnik GmbH). The pump allows the liquid pressure and flow rate to be controlled independently. The liquid pressure is controlled through adjusting the applied voltage, while the

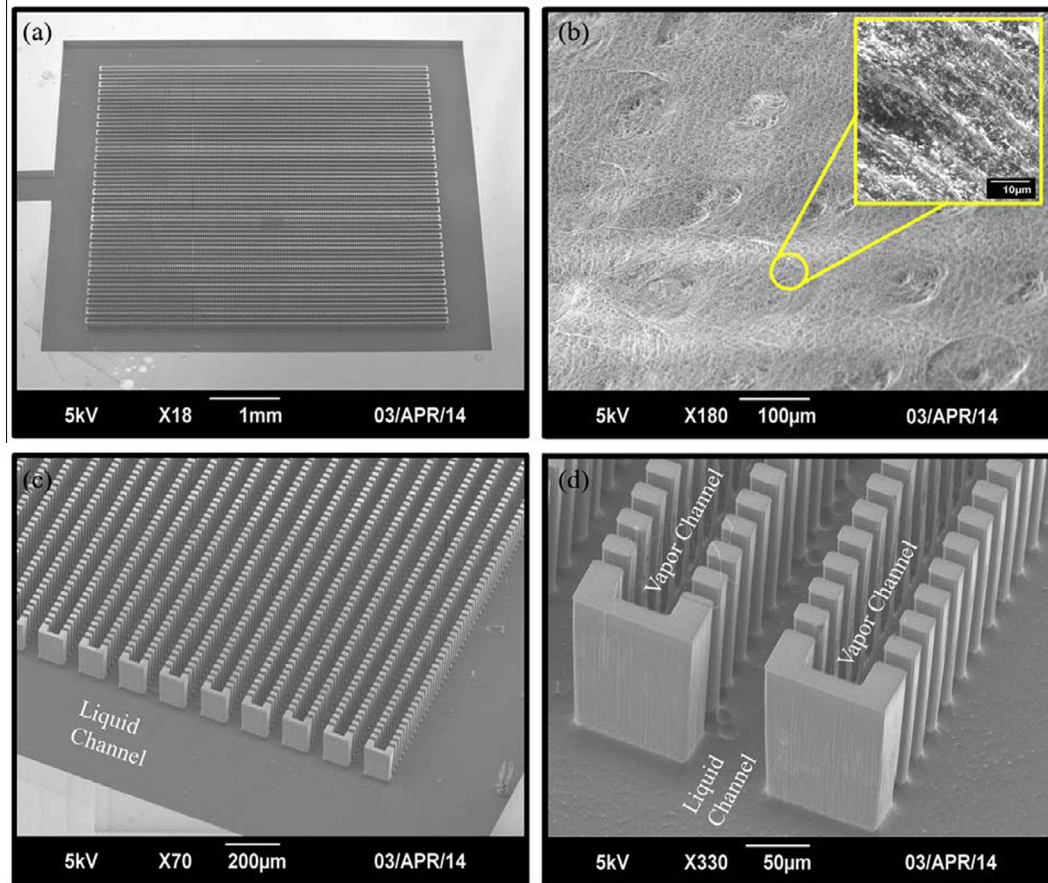


Fig. 6. SEM images of the heat sink. (a) Isometric view of the device showing its active area (the area with fins) surrounded by a trench connected to a liquid inlet. (b) A porous PTFE membrane bonded over the fins (the inset figure shows a close view of the membrane fibrous structure). (c) A top view of the device showing the surface microstructures. (d) A close view of the surface structures showing the liquid and vapor channels.

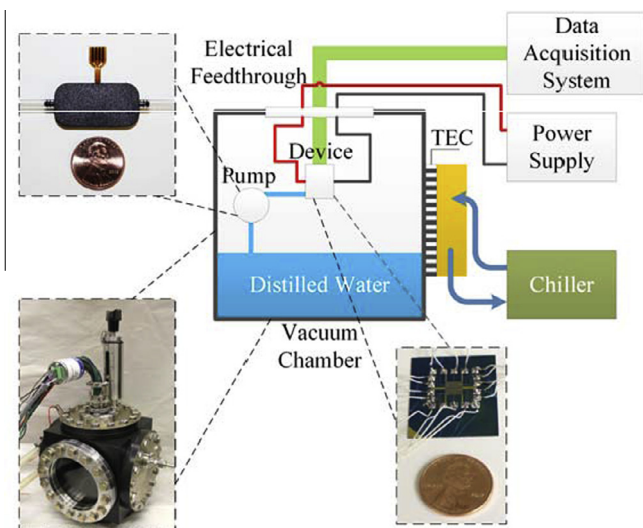


Fig. 7. A schematic of the experimental setup used for diabatic tests.

liquid flow rate is changed through adjusting the frequency. Two pressure transducers (Setra 730) are utilized to measure the chamber and the heat sink inlet pressures. The reported ΔP at each test is the difference between the two measured pressure values. The heat sink is designed such that the pressure drop in the liquid

microchannels is an order of magnitude lower than the pressure difference across the menisci. Hence, the liquid pressure at the menisci is almost equal to the liquid inlet pressure. An Agilent data acquisition system is used for recording the pressure and temperature of the chamber and the device. The generated vapor during the device operation is condensed by a thermoelectric cooler (TEC) and returns back to the water reservoir.

To accurately measure the surface heat flux, the device heat loss is measured as a function of its temperature. The heat loss occurs through heat dissipation to the device ambient, and the wiring system that connects the device heaters and sensors to a set of terminals. This measurement is conducted while the heat sink is dry. The energy supplied to the device to maintain it at a set temperature is considered to be its heat loss. The heat flux is calculated based on the heat sink base area.

Water is used as the working fluid in all experiments. The thermo-physical properties of water used in the numerical simulations are listed in Table 2.

Table 2
Thermophysical properties of water at saturation condition.

Thermal conductivity, k_f (W/m K)	0.679
Specific heat capacity, $C_{p,f}$ (kJ/kg K)	4.216
Density, ρ_f (kg/m ³)	958.4
Surface tension, σ_f (mN/m)	71.97

Table 3
Uncertainty of different instruments.

Variable	Uncertainty (%)
Pressure	±0.50
Voltage	±0.05
Current	±0.20
Heated area	±0.20

4.3. Uncertainty analysis

The temperature sensors are calibrated using an OMEGA HSRTD-3-100-A-80-E probe and measurement system with an overall uncertainty of $\pm(0.15 + 0.002T)$. The temperature uncertainty varies from ± 0.37 °C at 100 °C to ± 0.44 °C at 135 °C (the uncertainty in measurement of the sensors resistance is responsible for a higher uncertainty compared to the reference temperature probe). The uncertainties associated with other instruments are listed in Table 3 (obtained from the manufacturer's datasheet).

The uncertainty associated with heat dissipation through phase change process (Q_{diss}) is due to uncertainty in the total heat applied to the device (Q_{total}) and the heat loss through mechanisms discussed in the previous section (Q_{loss}). Eq. (9) provides the relation between the different introduced heat terms.

$$Q_{diss} = Q_{total} - Q_{loss} \quad (9)$$

The uncertainty associated with $Q_{total}(= V \times I)$ is $\pm 0.21\%$, determined using the following expression.

$$\frac{\delta Q_{total}}{Q_{total}} = \sqrt{\left(\frac{\delta V}{V}\right)^2 + \left(\frac{\delta I}{I}\right)^2} \quad (10)$$

In order to calculate the uncertainty in Q_{loss} , the heat loss calibration data are correlated to the difference between the temperature of the device (T_s) and its surrounding environment (T_{sur}) using the following expression.

$$Q_{loss} = m(T_s - T_{sur}) \quad (11)$$

The value of m is 0.0353 ± 0.0008 W/°C determined using a linear fit to the heat loss (Q_{loss}) versus the temperature difference ($T_s - T_{sur}$) data. This expression is later used to estimate the heat loss at each test condition. The uncertainty associated with this estimation is calculated using the expression provided below. It should be noted that the uncertainty associated with measurement of T_{sur} is ± 0.35 °C (measured using the OMEGA temperature probe) while the measurement uncertainty of T_s varies as mentioned earlier.

$$\frac{\delta Q_{loss}}{Q_{loss}} = \sqrt{\left(\frac{\delta m}{m}\right)^2 + \left(\frac{\delta(T_s - T_{sur})}{T_s - T_{sur}}\right)^2} \quad (12)$$

where

$$\frac{\delta(T_s - T_{sur})}{T_s - T_{sur}} = \sqrt{\left(\frac{\delta T_s}{T_s - T_{sur}}\right)^2 + \left(\frac{\delta T_{sur}}{T_s - T_{sur}}\right)^2} \quad (13)$$

Hence, the uncertainty associated with estimating the Q_{loss} ranges from $\pm 56.8\%$ (or ± 0.018 W) to $\pm 2.8\%$ (or ± 0.034 W) when the surface temperature is changed from 100.5 °C to 135 °C. Using the Q_{total} and Q_{loss} uncertainties, the uncertainty in Q_{diss} is determined using Eq. (14). This uncertainty varies from $\pm 1.46\%$ to $\pm 0.21\%$ when the surface temperature is increased from 100.5 °C to 135 °C.

$$\frac{\delta Q_{diss}}{Q_{diss}} = \sqrt{\left(\frac{\delta Q_{total}}{Q_{diss}}\right)^2 + \left(\frac{\delta Q_{loss}}{Q_{diss}}\right)^2} \quad (14)$$

The uncertainty in the reported heat flux ($q'' = Q_{diss}/A$), determined using Eq. (15), changes from $\pm 1.47\%$ to $\pm 0.29\%$ with increasing the surface temperature from 100.5 °C to 135 °C.

$$\frac{\delta q''}{q''} = \sqrt{\left(\frac{\delta Q_{diss}}{Q_{diss}}\right)^2 + \left(\frac{\delta A}{A}\right)^2} \quad (15)$$

The uncertainty in the heat transfer coefficient can then be calculated using the following equation.

$$\frac{\delta h}{h} = \sqrt{\left(\frac{\delta q''}{q''}\right)^2 + \left(\frac{\delta(\Delta T)}{\Delta T}\right)^2} \quad (16)$$

Here, ΔT is the difference between the surface and saturation temperatures. The saturation temperature values are calculated with an uncertainty of ± 0.15 °C using the pressure data recorded by Setra 730 pressure transducer. The overall uncertainty in ΔT is determined to be ± 0.40 °C and ± 0.46 °C at 100.5 °C and 135 °C, respectively. Finally, the heat transfer coefficient uncertainty is found to be $\pm 44.4\%$ at the lowest recorded wall superheat of 0.9 °C. The uncertainty then drops to $\pm 5.2\%$ and $\pm 1.4\%$ at 8 °C and 30 °C wall superheats, respectively.

Each test was conducted for at least four times to ensure the repeatability of the presented data. The temperature value reported for each test is the average of over 200 data points recorded at each test point.

$$T_s = \sum_{j=1}^k \bar{T}_j / k, \quad k \geq 4 \quad (17)$$

where $\bar{T}_j = \sum_{i=1}^N T_{ij}/N, N \geq 200$

The heat flux values are similarly averaged, as shown below.

$$q'' = \sum_{j=1}^k q''_j / k, \quad k \geq 4 \quad (18)$$

5. Results and discussions

5.1. Hydraulic characteristics

The adiabatic test setup is used to study the liquid–vapor interface position at different pressures. At a low pressure ($\Delta P_1 \sim 4$ kPa), the interface curvature, as shown in Fig. 8a, is small and surface tension forces balance out the forces applied by the liquid pressure. Increasing the liquid pressure ($\Delta P_2 \sim 6.1$ kPa) enhances the meniscus curvature and expands the contact area between the liquid and the posts sidewalls (cf. Fig. 8a). The meniscus, which is still pinned to the top and bottom of the wall, starts to curve and moves forward to compensate for the increased liquid pressure. Further increase in the liquid pressure ($\Delta P_3 \sim 9.8$ kPa) unpins the interface from the top and bottom surfaces and result in an advancement of the meniscus into the gap until it is pinned from the left and right sides at the end of the gap. When the liquid pressure reaches a critical value (burst pressure), increasing the curvature (i.e. reducing the radius of curvature) is no longer enough to cancel out the pressure forces. Therefore, the meniscus breaks and the liquid flows into the vapor channel.

Fig. 8b shows the entire interface at three different pressures determined using numerical simulations. The numerical model predicts the overall shape and position of the meniscus reasonably well. It should be noted that some difference between the experimental and numerical results could have arisen due to the scallop pattern formed on the pillars sidewalls during the deep reactive ion etching (DRIE) process [33]. To evaluate the accuracy of the numerical simulation in predicting the meniscus curvature, a Matlab code was written to reconstruct the interface using the

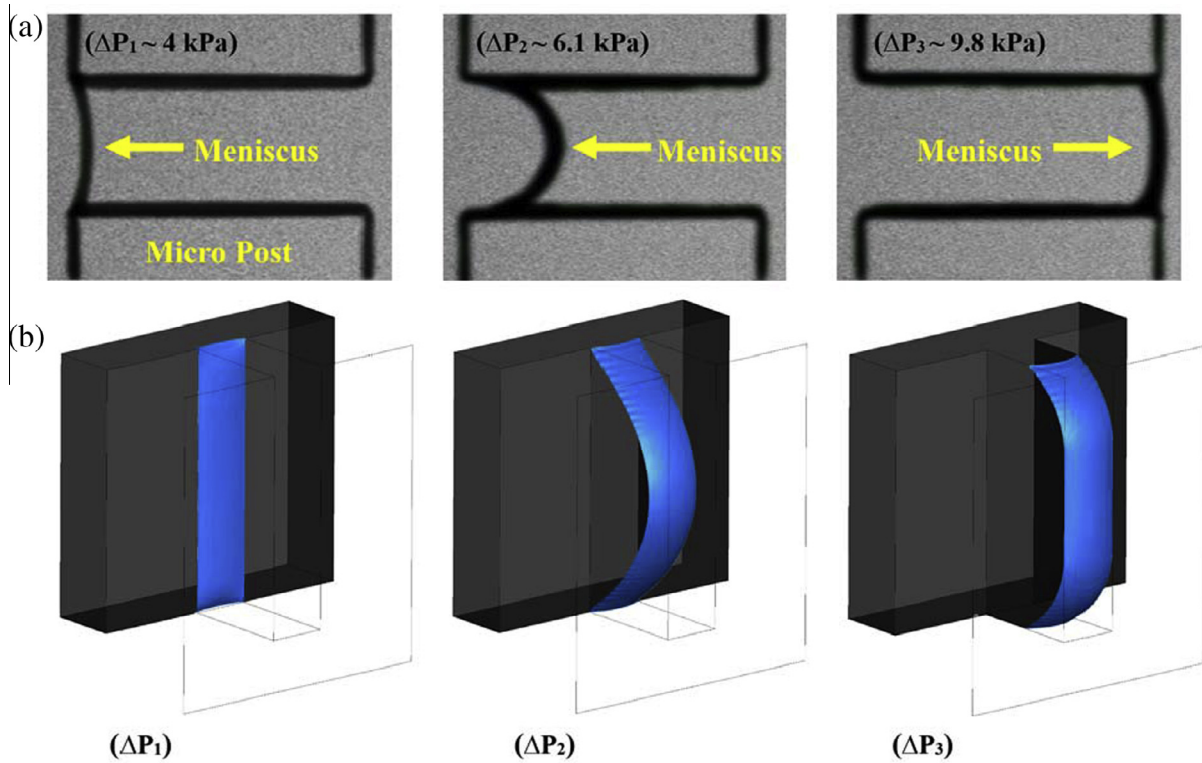


Fig. 8. Effect of supplied pressure on the meniscus. (a) Experimental visualization (top view at the middle of microchannel, $z = 75 \mu\text{m}$) (b) Numerical simulations (isometric view).

numerical data. To calculate the pressure difference across the meniscus using the Young–Laplace equation, the principle curvatures (κ_1 and κ_2), mean (H) and Gaussian (K) curvatures are first calculated, using the following equations:

$$K = \kappa_1 \kappa_2 = \frac{F_{xx}F_{yy} - F_{xy}^2}{(1 + F_x^2 + F_y^2)^2} \quad (19)$$

$$H = \frac{1}{2}(\kappa_1 + \kappa_2) = \frac{F_{xx}(1 + F_y^2) - 2F_{xy}F_xF_y + F_{yy}(1 + F_x^2)}{2(1 + F_x^2 + F_y^2)^{3/2}} \quad (20)$$

where $z = F(x, y)$ is the fifth order polynomial fitted to the experimental data to reconstruct the meniscus. The principle curvatures and radii of curvatures can then be calculated using the following equations.

$$\kappa_{1,2} = H \pm \sqrt{H^2 - K} \quad (21)$$

$$R_{1,2} = \frac{1}{\kappa_{1,2}} \quad (22)$$

The principle radii of curvature were then used to determine pressure difference across the interface using the Young–Laplace equation (Eq. (1)). Table 4 lists the average principle radii of

Table 4
Comparison of the applied and calculated pressures.

ΔP (kPa)	R_1 (μm)	R_2 (μm)	Calculated ΔP (kPa)
9.8	5.13	56.82	10.25
6.1	8.03	74.07	6.65
4.0	12.38	107.53	4.34

curvature for the menisci shown in Fig. 8b and compares the calculated and applied pressures. The calculated pressure values are within $\sim 10\%$ of the measured values.

5.2. Thermal characterization

Fig. 9 presents the device thermal performance at different supplied liquid pressures. As mentioned, when the supplied liquid

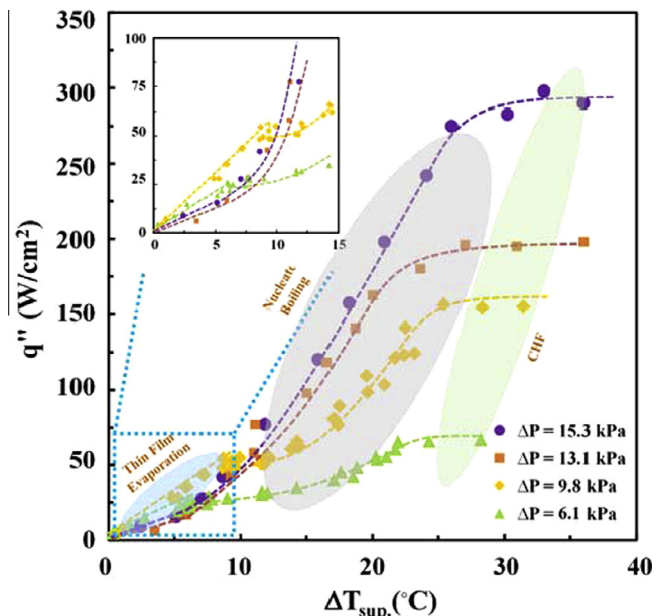


Fig. 9. Heat flux data as a function of wall superheat at different supplied liquid pressures.

pressure is below the meniscus breakthrough pressure (~ 11 kPa), a stable liquid–vapor interface forms between the liquid and vapor channels. Upon heating, the liquid evaporates into the vapor channels and subsequently exits the device through the membrane. In this operation mode, heat transfer is dominated by thin film evaporation and an almost linear relation between the heat flux and the wall superheat is observed (cf. inset in Fig. 9). Further increase of the wall superheat temperature resulted in the onset of nucleation and a sudden change in the heat flux versus the temperature curve (cf. Fig. 9).

When the liquid pressure is increased beyond the limit predicted by the Young–Laplace equation (i.e. $\Delta P > \sim 11$ kPa), the liquid–vapor interface breaks down and the liquid floods the entire structure. Under this condition, at low wall superheats, heat is removed through direct evaporation of the liquid at the liquid–membrane interface. During the boiling operating mode, the liquid pressure limits the bubbles expansion and results in their discharge through the membrane. As a result, increasing the pressure directly enhances the CHF while the heat sink exit quality always remains at 100%. The remainder of this section is dedicated to a comprehensive analysis of the thin film evaporation mode of the heat sink.

The temperature contours of the liquid and vapor phases as well as the particle trajectories at a liquid pressure of 4 kPa are presented in Fig. 10. The liquid–vapor interface is formed at the entrance of the gap between the micro-pillars. The interface temperature remains constant and equal to the saturation temperature due to the liquid evaporation. The temperature of the liquid behind the interface is higher than the saturation temperature establishing a temperature gradient within the liquid phase. As will be shown later, the maximum temperature gradient and associated evaporation rate occurs near the triple line. A higher evaporation rate near the triple line leads to a 3D helical flow stream in the liquid phase, as indicated by the particle trajectories shown in Fig. 10b.

Fig. 11a shows the steady-state temperature distribution at different liquid pressures at $y = 75 \mu\text{m}$. As mentioned previously, the

liquid–vapor interface advances further inside the gap within the surface structures as the liquid pressure is increased. As can be seen in Fig. 11a, the high temperature region behind the interface expands as more liquid comes into contact with the solid walls. Consequently, the temperature gradient at the interface that dictates the heat dissipation rate increases. Fig. 11b shows the local wall heat flux variations over the micro-pillars sidewalls. At the gap entrance, the thermal boundary layer is thin resulting in a high heat flux (cf. point A in Fig. 11b). As the thermal boundary layer grows with distance from the gap entrance, the local heat flux over the sidewall drops (cf. region A–B in Fig. 11b). Since the evaporation process occurs over the interface, the local heat flux experiences a spike at the interface (cf. point C in Fig. 11b). After this heat flux peak, the surface heat flux suddenly drops due to the low thermal conductivity of the vapor phase. Fig. 11c shows the heat flux variations over the fins sidewalls at different pressures. At low pressure ($\Delta P = 4$ kPa), the meniscus is formed very close to the gap entrance. As a result, the high heat flux associated with the gap entrance (cf. point A in Fig. 11b) and the heat flux spike associated with the interface (cf. point C in Fig. 11b) merge into a single maximum value which then quickly reduces as vapor comes in contact with the wall. Increasing the liquid pressure pushes the liquid–vapor interface further inside the gap resulting in heat flux variations shown in Fig. 11c. Fig. 11c also shows that at higher liquid pressures, the liquid front advances within the microstructures resulting in an increase in the solid–liquid interface (i.e. wetted area) and consequently a higher heat transfer coefficient.

Local evaporative mass fluxes as a function of the non-dimensional meniscus length (X/L) at two different liquid pressures are provided in Fig. 11d. L represents the half distance between the micro-pillars. As expected, the evaporative mass flux is maximal in the vicinity of the wall ($X \sim 0$) and declines away from the solid wall, towards the middle of the gap. As the liquid pressure increases, the uniformity of the evaporative mass flux over the entire interface ($0 < X < L$) enhances. This is due to the fact that a more uniform temperature field behind the interface is obtained at higher liquid pressures (cf. Fig. 11a). In addition, the average

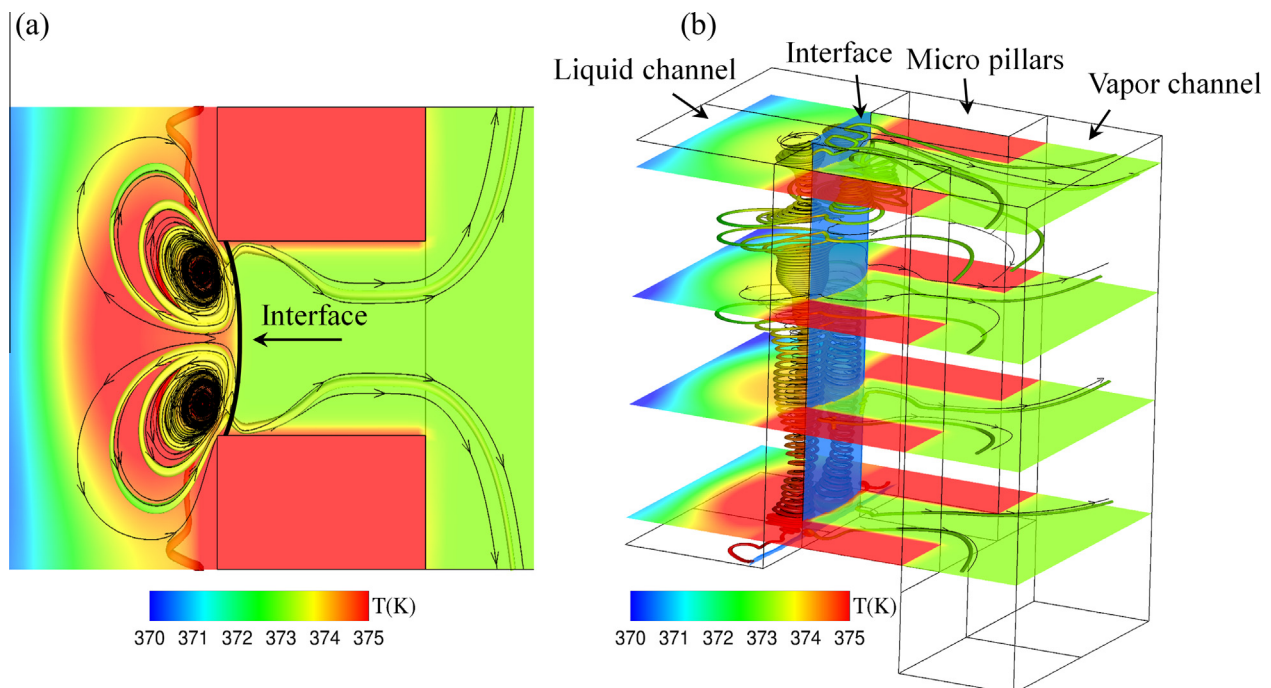


Fig. 10. Temperature contours and particle trajectories; (a) cross-sectional view and (b) 3D view.

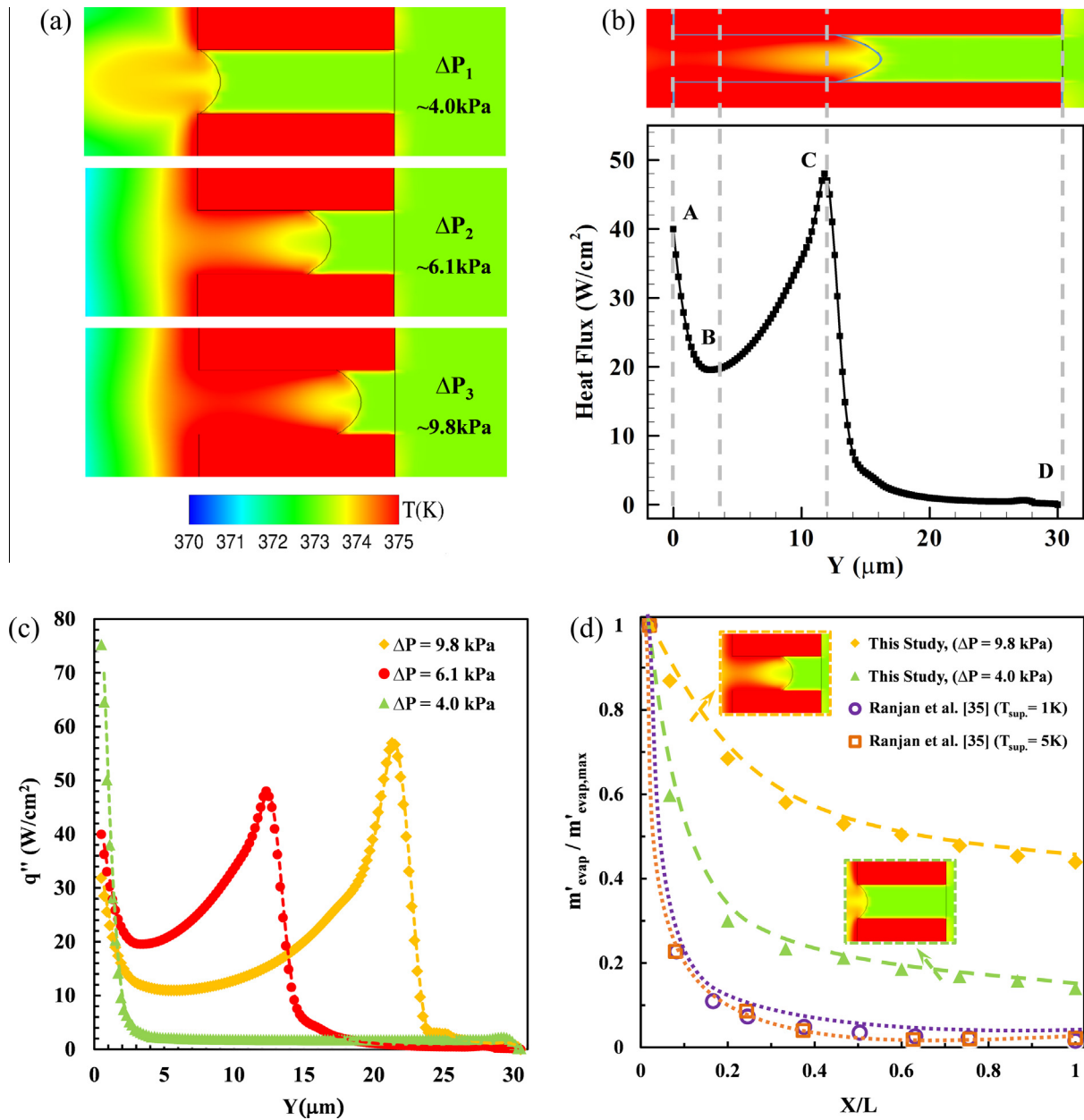


Fig. 11. (a) Steady state temperature distribution at different liquid pressures at $y = 75 \mu\text{m}$ ($\Delta P_3 > \Delta P_2 > \Delta P_1$), (b) Local wall heat flux variations over the side wall of the micro-pillars, (c) Wall heat flux variations over the side wall of the fins at different liquid pressures ($z = 50 \mu\text{m}$), and (d) Local evaporative mass flux over the liquid-vapor interface at different liquid pressures ($z = 50 \mu\text{m}$).

evaporative mass flux increases with the liquid pressure. Fig. 11d also presents evaporative mass fluxes over the interface of a capillary wick structure studied in Ref. [34]. In capillary wick structures, thin film evaporation is effective at regions very close to the hot walls and rapidly loses its efficiency away from the wall [35,36]. Ranjan et al. [34] reported up to 90% reduction in the evaporation rate within approximately 20% of meniscus length from the heated surface at 5 K superheat. In the present study, however, the results showed higher and more uniform evaporation rates over the entire liquid-vapor interface. At the optimal conditions, only 30% reduction in the evaporation rate was observed at the same length ratio reported by Ranjan et al. [34].

Fig. 12a compares the thin film evaporation data with the numerical results showing an overall agreement within 17%. As it can be seen, the heat flux steadily increases with the wall superheat temperature at a constant liquid pressure. By increasing the

liquid pressure, as mentioned earlier, the temperature gradient behind the meniscus intensifies leading to an increase in the heat flux at a constant wall superheat (cf. Fig. 12a). The difference between the numerical and experimental results could be mainly due to: (1) the actual liquid pressure distribution varies across the device whereas in the representative computational cell the inlet pressure is assumed to be equal to the device liquid supply pressure and (2) the micropillars walls are simulated with a perfectly smooth surface while the actual walls have a scallop pattern formed during the deep reactive ion etching (DRIE) process. Xiao et al. [33] showed that the effect of the scalloped features can be included in the simulations as an effective surface energy factor (the scallops were approximated as a series of semicircles with a roughness factor, $rf = \pi/2$).

Fig. 12b the heat transfer coefficient versus the surface temperature at different liquid inlet pressures. It can be seen that in the

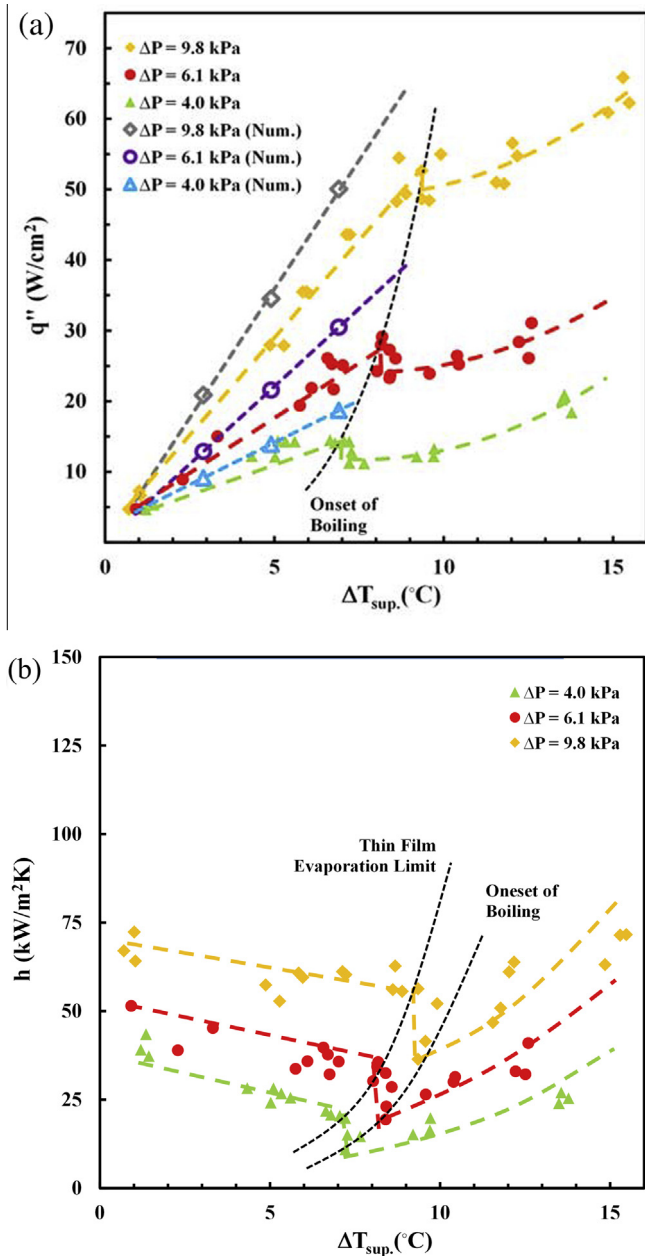


Fig. 12. Thermal performance of the device, (a) heat flux data as a function of the wall superheat at different supplied liquid pressures and (b) calculated heat transfer coefficients vs. wall superheat at different supplied liquid pressures.

thin film evaporation regime, the heat transfer coefficient increases with increasing the pressure since the liquid meniscus advances into the gap between the pillars, as shown in Fig. 11a. The heat transfer coefficient decreases with increasing the wall superheat temperature because the liquid–vapor interface within the gap recedes due to an increase in the water channel pressure drop. When boiling starts inside the device, the stable liquid–vapor interface breaks and heat transfer coefficient drops (cf. Fig. 12b).

6. Conclusion

A novel concept for two-phase heat sinks was introduced. The new heat sink operates at two different phase change modes. At low wall superheats, thin film evaporation is the primary mode of heat transfer while nucleate boiling heat transfer mode

dominates at high wall superheats. Unlike a typical two phase heat sink that requires at least a few degrees Celsius wall superheat temperature to reach nucleate boiling and its associated performance benefits (e.g. high heat transfer coefficient and low mass flux), the new heat sink concept can deliver a high heat transfer coefficient even at $<1^\circ\text{C}$ wall superheat and achieve 100% exit vapor quality. This alternative heat sink design takes advantage of capillary forces to maintain thin liquid layers between vertically oriented menisci across which the liquid is evaporated into neighboring vapor channels. A proof-of-concept device was fabricated and tested to demonstrate potential of the proposed design. A maximum heat flux of 54 W/cm^2 was achieved at approximately 8°C wall superheat temperature, corresponding to a heat transfer coefficient of approximately $62\text{ kW/m}^2\text{K}$. The device performance in this mode was analyzed using numerical simulations. It was shown that the thermo-hydraulic characteristics of the heat sink can be adjusted with the liquid pressure. The applied pressure dictates the shape and location of the meniscus formed within the microstructure. The device thermal performance at the thin film evaporation mode can be improved by increasing the microstructures height, which linearly enhances the liquid–solid contact area as well as the liquid–vapor interface. Increasing the wall superheat temperature to $7\text{--}9^\circ\text{C}$ activated the nucleation sites and resulted in transition to the boiling regime. At this mode, the liquid–vapor interface breaks down and liquid floods the entire device. In the boiling mode, bubbles are subjected to an omnidirectional pressure that limits their lateral expansion over the heat transfer surface. Then, the bubbles are removed from the heated surface through the vapor permeable membrane. Heat flux dissipation rates of up to 300 W/cm^2 were obtained at wall superheats of $<30^\circ\text{C}$.

References

- [1] C.C. Liu, A.K. Datta, S. Tiwari, Heating effects of clock drivers in bulk, SOI, and 3-D CMOS, *IEEE Electron Device Lett.* 23 (2002) 716–718.
- [2] E. Pop, S. Sinha, K.E. Goodson, Heat generation and transport in nanometer-scale transistors, *Proc. IEEE* 94 (2006) 1587–1601.
- [3] I. Mudawar, Assessment of high-heat-flux thermal management schemes, *IEEE Trans. Compon. Packag. Technol.* 24 (2001) 122–141.
- [4] P.E. Phelan, V.A. Chiriac, T.-Y.T. Lee, Current and future miniature refrigeration cooling technologies for high power microelectronics, *IEEE Trans. Compon. Packag. Technol.* 25 (2002) 356–365.
- [5] B. Agostini, M. Fabbri, J.E. Park, L. Wojtan, J.R. Thome, B. Michel, State of the art of high heat flux cooling technologies, *Heat Transfer Eng.* 28 (2007) 258–281.
- [6] M.B. Bowers, I. Mudawar, Two-phase electronic cooling using mini-channel and micro-channel heat sinks: Part 1—design criteria and heat diffusion constraints, *J. Electron. Packag.* 116 (1994) 290.
- [7] M.B. Bowers, I. Mudawar, High flux boiling in low flow rate, low pressure drop mini-channel and micro-channel heat sinks, *Int. J. Heat Mass Transfer* 37 (1994) 321–332.
- [8] X.F. Peng, B.X. Wang, G.P. Peterson, H.B. Ma, Experimental investigation of heat transfer in flat plates with rectangular microchannels, *Int. J. Heat Mass Transfer* 38 (1995) 127–137.
- [9] C.-J. Kuo, Y. Peles, Local measurement of flow boiling in structured surface microchannels, *Int. J. Heat Mass Transfer* 50 (2007) 4513–4526.
- [10] R. Chen, M. Lu, V. Srinivasan, Z. Wang, H.H. Cho, A. Majumdar, Nanowires for enhanced boiling heat transfer, *Nano Lett.* 9 (2009) 548–553.
- [11] M.P. David, J. Miller, J.E. Steinbrenner, Y. Yang, M. Touzelbaev, K.E. Goodson, Hydraulic and thermal characteristics of a vapor venting two-phase microchannel heat exchanger, *Int. J. Heat Mass Transfer* 54 (2011) 5504–5516.
- [12] D. Li, G.S. Wu, W. Wang, Y.D. Wang, D. Liu, D.C. Zhang, et al., Enhancing flow boiling heat transfer in microchannels for thermal management with monolithically-integrated silicon nanowires, *Nano Lett.* 12 (2012) 3385–3390.
- [13] A. Fazeli, M. Mortazavi, S. Moghaddam, Hierarchical biphilic micro/nanostructures for a new generation phase-change heat sink, *Appl. Therm. Eng.* 78 (2015) 380–386.
- [14] A. Fazeli, S. Moghaddam, Microscale phase separator for selective extraction of CO₂ from methanol solution flow, *J. Power Sources* 271 (2014) 160–166.
- [15] S. Moghaddam, Microscale Study of Nucleation Process in Boiling of Low-Surface-Tension Liquids, University of Maryland, 2006.
- [16] S. Moghaddam, K. Kiger, Physical mechanisms of heat transfer during single bubble nucleate boiling of FC-72 under saturation conditions-I. Experimental investigation, *Int. J. Heat Mass Transfer* 52 (2009) 1284–1294.
- [17] S. Moghaddam, K. Kiger, Physical mechanisms of heat transfer during single bubble nucleate boiling of FC-72 under saturation conditions. II: theoretical analysis, *Int. J. Heat Mass Transfer* 52 (2009) 1295–1303.

- [18] J. Kim, Review of nucleate pool boiling bubble heat transfer mechanisms, *Int. J. Multiphase Flow* 35 (2009) 1067–1076.
- [19] S.R. Rao, F. Houshmand, Y. Peles, Transient flow boiling heat-transfer measurements in microdomains, *Int. J. Heat Mass Transfer* 76 (2014) 317–329.
- [20] S. Bigham, S. Moghaddam, Microscale study of mechanisms of heat transfer during flow boiling in a microchannel, *Int. J. Heat Mass Transfer* 88 (2015) 111–121.
- [21] F. Gibou, L. Chen, D. Nguyen, S. Banerjee, A level set based sharp interface method for the multiphase incompressible Navier–Stokes equations with phase change, *J. Comput. Phys.* 222 (2007) 536–555.
- [22] S. Tanguy, M. Sagan, B. Lalanne, F. Couderc, C. Colin, Benchmarks and numerical methods for the simulation of boiling flows, *J. Comput. Phys.* 264 (2014) 1–22.
- [23] M. Sussman, P. Smereka, S. Osher, A level set approach for computing solutions to incompressible two-phase flow, *J. Comput. Phys.* 114 (1994) 146–159.
- [24] S. Osher, J.A. Sethian, Fronts propagating with curvature-dependent speed: Algorithms based on Hamilton–Jacobi formulations, *J. Comput. Phys.* 79 (1988) 12–49.
- [25] R.P. Fedkiw, T. Aslam, B. Merriman, S. Osher, A Non-oscillatory eulerian approach to interfaces in multimaterial flows (the ghost fluid method), *J. Comput. Phys.* 152 (1999) 457–492.
- [26] C. Hirt, B. Nichols, Volume of fluid (VOF) method for the dynamics of free boundaries, *J. Comput. Phys.* 39 (1981) 201–225.
- [27] W.J. Rider, D.B. Kothe, Stretching and tearing interface tracking methods, in: *AIAA 12th Comput. Fluid Dyn. Conf.*, 1995: pp. 806–810.
- [28] J.E. Pilliod, E.G. Puckett, Second-order accurate volume-of-fluid algorithms for tracking material interfaces, *J. Comput. Phys.* 199 (2004) 465–502.
- [29] J. Li, Piecewise linear interface calculation. Technical report, *Comptes Rendus de l'Academie des Sciences Serie II. Fascicule B-Mecanique*, 1995.
- [30] D. Gueyffier, J. Li, A. Nadim, R. Scardovelli, S. Zaleski, Volume-of-fluid interface tracking with smoothed surface stress methods for three-dimensional flows, *J. Comput. Phys.* 152 (1999) 423–456.
- [31] User's Guide for ANSYS FLUENT 12, Fluent Inc., 2009.
- [32] J. Brackbill, D. Kothe, C. Zemach, A continuum method for modeling surface tension, *J. Comput. Phys.* 100 (1992) 335–354.
- [33] R. Xiao, R. Enright, E.N. Wang, Prediction and optimization of liquid propagation in micropillar arrays, *Langmuir* 26 (2010) 15070–15075.
- [34] R. Ranjan, J.Y. Murthy, S.V. Garimella, A microscale model for thin-film evaporation in capillary wick structures, *Int. J. Heat Mass Transfer* 54 (2011) 169–179.
- [35] M.A. Hanlon, H.B. Ma, Evaporation heat transfer in sintered porous media, *J. Heat Transfer* 125 (2003) 644.
- [36] R. Ranjan, J.Y. Murthy, S.V. Garimella, Analysis of the wicking and thin-film evaporation characteristics of microstructures, *J. Heat Transfer* 131 (2009) 101001.
- [37] S. Bigham, S. Moghaddam, Role of bubble growth dynamics on microscale heat transfer events in microchannel flow boiling process, *Appl. Phys. Lett.* 107 (2015) 244103.